# Interaction between Hopf and static instabilities in a pattern-forming optical system

Yu. A. Logvin[1,2] and T. Ackemann[2]
[1]*Institute of Physics, Academy of Sciences, Skaryna Avenue 70, 220072 Minsk, Belarus*
[2]*Institut für Angewandte Physik, Westfälische Wilhelms-Universität Münster, Corrensstraße 2/4, D-48149 Münster, Federal Republic of Germany*

(Received 20 November 1997; revised manuscript received 17 April 1998)

Optical pattern formation in a spin-1/2 atomic system is theoretically studied in the situation of interaction between the Hopf and static instabilities. Variation of the parameters of the system permits a drastic change of the ratio between the spatial wave numbers of the Hopf and the static modes. If the mode coupling satisfies spatiotemporal phase matching conditions, regular patterns in the form of triadic Hopf-static patterns or oscillating patterns with hexagonal symmetry (''winking hexagons'') are formed. Otherwise, the simultaneous excitement of the Hopf and static modes leads to the development of spatiotemporal turbulence that is in agreement with results obtained in other systems. [S1063-651X(98)10504-4]

PACS number(s): 05.45.+b, 47.54.+r, 42.65.Sf, 82.40.Bj

## I. INTRODUCTION

In pattern-forming systems, several modes of different frequency and/or different modulus of wave vectors may simultaneously be active. In a rotational symmetric two-dimensional system there is in addition a degeneracy between all modes having wave vectors of the same modulus, i.e., forming a circle in Fourier space. We will call such a set of modes a ''family'' in the following. A resulting pattern will strongly be influenced by the development and interaction of modes of different families. In particular, resonant mode interaction permits us to explain pattern selection and metamorphoses in the Taylor-Dean system [1], in Rayleigh-Bénard convection of binary mixtures [2], and in the Brusselator model [3]. It has also been shown that stationary two-dimensional (2D) quasicrystals may be stabilized by a triadic coupling between modes from different families [4–7].

The excitation of several families of spatial modes (transverse to the direction of light propagation) is a striking generic feature of many pattern-forming nonlinear optical systems [7–11]. This is due to the properties of the diffraction operator which provides spatial transverse coupling within the propagating light beam and is the origin of the spatial instability. Therefore nonlinear optical systems can be considered to be particularly suitable to study pattern-forming processes involving modes from several families. It has recently been shown that—in addition to stationary structures [7,10,11]—nonstationary patterns named triadic Hopf-static patterns [12] and winking hexagons [13] occur in optical systems with a wide aperture feedback. The nonstationarity is caused by the circumstance that one of the unstable mode families (schematically shown by $\boldsymbol{k}_i$ in Fig. 1) originates from a Hopf type of instability whereas the family $\boldsymbol{q}_i$ is due to a static instability. It is clear from Fig. 1 that a spatiotemporal phase matching condition is fulfilled if the $\boldsymbol{k}_1$ mode has the Hopf frequency $\Omega$ and the $\boldsymbol{k}_2$ mode the frequency $-\Omega$ and if $\boldsymbol{k}_1+\boldsymbol{k}_2=\boldsymbol{q}_1$.

We consider a single-feedback-mirror system [9] with spin-1/2 atoms (modeling, e.g., sodium atoms in a buffer gas atmosphere of high pressure [14]) in an external magnetic field as a nonlinear medium. This combination already proved to be very suitable to study optical pattern formation experimentally and theoretically due to its versatility [13,15–18]. In this paper attention is paid to the spatiotemporal patterns which arise due to the interaction between Hopf and static modes. The suitable adjustment of the control parameters of the system—such as the external magnetic field and the frequency detuning between the incident light and the atomic transition—allows us to choose whether the Hopf or the static modes lie on the outer (or inner) circle of Fig. 1. This totally alters the phase matching conditions and thus the allowed interactions between the two mode families. We are not aware of any nonoptical system which allows such an easy exchange of the relative length scales of the two kinds of instabilities.

Numerical simulations permit us to conclude that regular spatiotemporal structures (triadic Hopf-static patterns and winking hexagons) exist when the mode coupling satisfies a phase matching condition and that spatiotemporal turbulence develops in the opposite case. It should be noted that the latter result matches the findings obtained for other, especially reaction-diffusion type, systems under conditions of the simultaneous development of Hopf and Turing modes [19–23].

## II. MODEL AND STABILITY OF HOMOGENEOUS SOLUTION

The model we are going to analyze was introduced in Refs. [15, 16] to describe the experimental observation of stationary patterns. It is based on the quantum mechanical equation of motion for the Bloch vector $\boldsymbol{m}=(u,v,w)$ describing the dynamics of the magnetization in the sodium ground state [15,14]:

$$\partial_t \boldsymbol{m} = -(\gamma - D\Delta_\perp + P)\boldsymbol{m} - \boldsymbol{m}\boldsymbol{\Omega} + \hat{\boldsymbol{e}}_z P \tag{1}$$

and the classical paraxial wave equation for the light propagation [8,9]. In Eq. (1), $\gamma$ is the collision induced relaxation of $\boldsymbol{m}$, $D$ is the diffusion constant, $\Delta_\perp$ is the transverse part of the Laplacian, $P$ denotes the optical pump rate. The vector $\boldsymbol{\Omega}=(\Omega_x,0,\Omega_z-\overline{\Delta}P)$ is an effective torgue vector [14] which

 

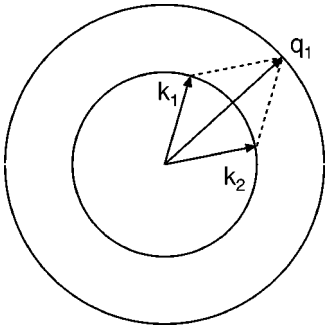


FIG. 1. Schematic diagram illustrating the resonant coupling of modes from two different families.

is composed not only from the Larmor frequencies $\Omega_x$ and $\Omega_z$ of the external magnetic field components, but it contains the light intensity dependent term $\bar{\Delta}P$ originating from the light shift ([18], and references therein). $\bar{\Delta}$ is the detuning between the incident field and the atomic transition, normalized to the relaxation constant $\Gamma_2$ of the polarization of the medium. The pump rate $P$ is taken to be proportional to the sum of the intensities of the forward ($E_0$) and the backward ($E_b$) waves:

$$P=(|E_0|^2+|E_b|^2)|\mu_e|^2/4\hbar^2\Gamma_2(\bar{\Delta}^2+1). \tag{2}$$

The backward field is given by

$$E_b=\sqrt{R}e^{-id\Delta_\perp/k}E_t, \tag{3}$$

where $E_t=E_0\exp(-i\chi kl/2)$ is the transmitted field ($\chi$ is the susceptibility of the sodium vapor, $k$ is the wave number of light in vacuum, $l$ is the length of nonlinear medium). The exponential factor stands for the formal solution of the paraxial wave equation describing light propagation in free space of length $d$ between the cell and the mirror with reflection coefficient $R$.

The susceptibility is coupled to the longitudinal component of the orientation of the sodium ground state $w\equiv m_z$ through [14]

$$\chi=-\frac{N|\mu_e|^2}{2\hbar\epsilon_0\Gamma_2}\frac{\bar{\Delta}+i}{\bar{\Delta}^2+1}(1-w)\equiv\chi_{\mathrm{lin}}(1-w), \tag{4}$$

where $N$ is the sodium particle density.

The steady-state homogeneous solution $\boldsymbol{m}_s=(u_s,v_s,w_s)$ of Eq. (1) is given by the expressions for the first two Bloch vector components,

$$u_s=\frac{(\Omega_z-\bar{\Delta}P_s)\Omega_x}{(\Omega_z-\bar{\Delta}P_s)^2+(\gamma+P_s)^2}w_s, \tag{5}$$

$$v_s=-\frac{(1+P_s)\Omega_x}{(\Omega_z-\bar{\Delta}P_s)^2+(\gamma+P_s)^2}w_s, \tag{6}$$

and a nonlinear algebraic equation for the orientation $w_s$,

$$w_s=\frac{P_s}{\gamma+P_s}\frac{(\Omega_z-\bar{\Delta}P_s)^2+(\gamma+P_s)^2}{(\Omega_z-\bar{\Delta}P_s)^2+(\gamma+P_s)^2+\Omega_x^2}, \tag{7}$$

with $P_s=P_0\{1+R|\exp[-ikl\chi_{\mathrm{lin}}(1-w_s)/2]|^2\}$. Here $P_0$ denotes the pump rate introduced by the forward beam ($P_0\sim|E_0|^2$) which is referred to as a control parameter.

A linear stability analysis with respect to a spatially inhomogeneous perturbation proportional to $\exp(\eta t+i\boldsymbol{k}_\perp\cdot\boldsymbol{r}_\perp)$ yields a cubic equation for the growth exponent $\eta$:

$$\eta^3+a_2\eta^2+a_1\eta+a_0=0, \tag{8}$$

with the coefficients $a_i$ given in the Appendix. A bifurcation is referred to as stationary if there are real roots $\eta_i$ larger than zero. In the case of a pair of complex conjugated roots with positive $\mathrm{Re}(\eta_i)$ we deal with a Hopf bifurcation. The condition of the Hopf bifurcation is determined by the coefficients of Eq. (8): $a_i>0$ and $a_1a_2-a_0<0$.

It is instructive to note here that, since the diffractive coupling is determined by the operator $\exp(-id\Delta_\perp/k)$ in Eq. (3), the coefficients $a_i$ depend on the diffraction parameter $dk_\perp^2/k$ acting as the argument of the trigonometric sine and cosine functions. Obviously, extremal values for the coefficients $a_i$ are achieved for $\sin(dk_\perp^2/k)=\pm1$, or

$$\frac{dk_\perp^2}{k}=\left(\frac{1}{2}+m\right)\pi, \tag{9}$$

where $m$ is integer. (The influence of the cosine term is not important in the case of a large detuning parameter $\bar{\Delta}$.) This circumstance has already been noted in the earliest study of the single-feedback-mirror model [8] and can be interpreted from the viewpoint of the Talbot effect [24]. Even values of $m$ correspond to a self-focusing situation, i.e., the refractive index

$$n(P)=1-\frac{N|\mu_e|^2}{4\hbar\epsilon_0\Gamma_2}\frac{\bar{\Delta}}{\bar{\Delta}^2+1}[1-w(P)] \tag{10}$$

increases for increasing pump rate, while odd values of $m$ correspond to a self-defocusing situation. This difference in length scale selection will be of great importance in the study of the pattern formation below.

Equation (9) indicates that there are in principle an infinite number of unstable modes equally spaced on the $k_\perp^2$ axis. For vanishing diffusion these modes are all degenerate, while for a nonzero diffusion coefficient the threshold increases for increasing modulus of the wave vector. As is apparent from the form of Eq. (1) in Fourier space the principal dependence of the growth rate $\eta$ on $D$ is $\eta\approx-Dk_\perp^2+\cdots$ [9,16]. Thus by choosing the cell-to-mirror distance $d$, which determines $k_\perp$ [cf. Eq. (9)], one can tune the difference in growth rate between modes with different $m$ (for given values of the diffusion coefficient and the other atomic parameters).

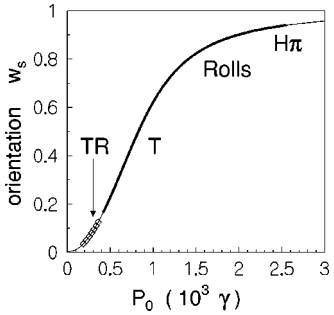


FIG. 2. Steady-state orientation $w_s$ versus pump rate produced by the external light beam for the parameters $\bar{\Delta}=13$, $R=0.915$, $l=15$ mm, $\Omega_x/2\pi=15$ kHz, $\Omega_z/2\pi=0$, $N=1.2\times10^{14}$ cm$^{-3}$, $\gamma=6$ sec$^{-1}$, $\Gamma_2/2\pi=1.8\times10^9$ sec$^{-1}$, $\mu_e=1.72\times10^{-29}$ Cm. The interval with a static instability is marked by a thick solid line for a distance between the cell and the mirror of $d=800$ mm and a diffusion parameter of $D=40$ mm$^2$/s. Diamonds denote the domain displaying a Hopf bifurcation. Patterns observed in numerical simulations: *TR*—traveling rectangles, *T*—turbulence, *R*—roll or stripe pattern, *H*$\pi$—negative hexagons.

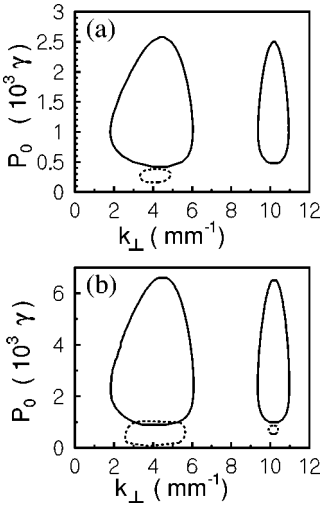


FIG. 3. Neutral stability curves in the plane $(P_0,k_\perp)$. (a) Parameters are the same as in Fig. 2. (b) $\bar{\Delta}=16$, $N=1.4\times10^{14}$ cm$^{-3}$, $\Omega_x/2\pi=45$ kHz, other parameters as in Fig. 2. The domains of the static (Hopf) instability are bounded by solid (dashed) lines.

## III. RESULTS AND DISCUSSION

Depending on the parameters (namely, on the external magnetic field and detuning $\bar{\Delta}$) the system can behave in various ways. Below we consider several typical examples of behavior.

### A. Zero longitudinal magnetic field: $\Omega_z=0$

In the absence of a longitudinal magnetic field, the expression for the steady-state orientation takes the form

$$w_s=\frac{P_s}{\gamma+P_s}\,\frac{(\bar{\Delta}P_s)^2+(\gamma+P_s)^2}{(\bar{\Delta}P_s)^2+(\gamma+P_s)^2+\Omega_x^2}. \tag{11}$$

As is apparent from Eq. (11), $w_s$ grows monotonically from 0 to 1 with increasing pump rate. Since $\gamma$ is assumed to be much smaller than the transverse magnetic field (which is the experimentally relevant situation), the growth rate is determined by $\Omega_x$. A typical example of such a behavior is presented in Fig. 2. The steady-state characteristic is not sensitive to a change of the sign of the detuning $\bar{\Delta}$ [cf. Eq. (11)]. In contrast, the length scales of the developing patterns are different on both sides of the resonance [cf. Eq. (9)].

With the help of a linear stability analysis, we find partitions of the steady-state characteristic where the homogeneous solution is unstable versus pattern formation. Such partitions are marked by a thick solid line (static type of instability) or diamonds (Hopf instability) in Fig. 2. Figure 3 shows the marginal stability curves for two sets of parameters: Fig. 3(a) corresponds to the case of Fig. 2 and Fig. 3(b) is produced for the case of larger values of the detuning and the transverse magnetic field. For the static as well as for the Hopf instability (if present), the wave numbers for the domains in Fig. 3 differ approximately by a factor of $\sqrt{5}$, which is in accordance with the prediction by Eq. (9) (i.e., $m=0$ for the left domain, and $m=2$ for the right one). The regions with the static and Hopf instabilities can overlap as in Fig. 3(b) or not [Fig. 3(a)], i.e., one is in the vicinity of a codimension-2 bifurcation point. Immediately at the threshold of the Hopf bifurcation, the frequency of the oscillations $\Omega_H$ coincides (within a few percent) with the Larmor frequency $\Omega_x$ of the transverse magnetic field. Beyond threshold, the Hopf frequency decreases with increasing pump as shown in Fig. 4.

The physical origin of the oscillations is the Larmor precession of the magnetization vector in the external magnetic field [cf. the cross product in Eq. (1)]. Without feedback the oscillations are damped but can become undamped by the feedback. Similar oscillations (but homogeneous) are known to occur in nonlinear resonators filled with an alkaline vapor and were named *magnetically induced self-oscillations* [14,25–27].

Analytical results can give only limited information about the behavior of the system. In order to obtain the full picture, numerical simulations are necessary. As in previous work [13,15–17] we have used an explicit difference scheme to integrate the material equations (1) and a fast Fourier transform algorithm to treat the propagation of the light field in free space [Eq. (3)]. Periodic boundary conditions have been assumed. The spatial mesh typically consisted of $128\times128$

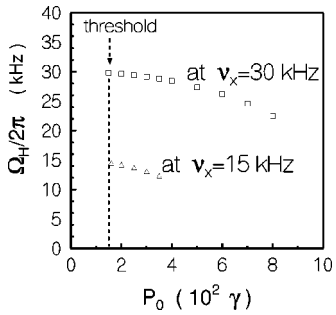


FIG. 4. The dependence of the Hopf frequencies on the external pump rate as calculated from the linear stability analysis for $\Omega_x/2\pi=15$ kHz (triangles) and $\Omega_x/2\pi=30$ kHz (squares). All other parameters are as in Fig. 3(a).

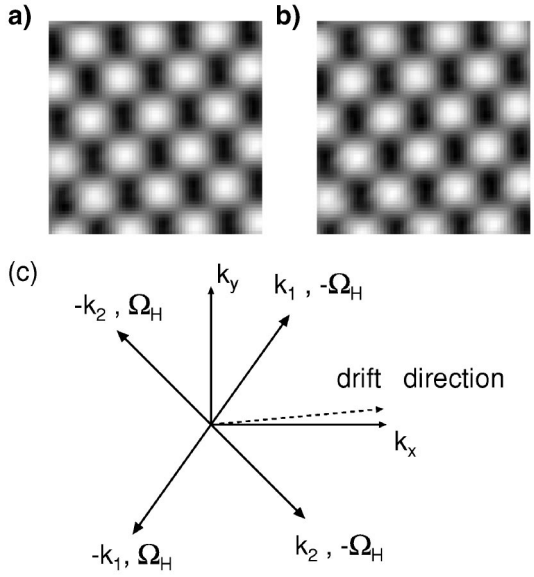


FIG. 5. (a) and (b) are two snapshots of a traveling rectangle structure with the temporal interval between them being half a period. The images are in a gray-level coding. White corresponds to high levels of the orientation. The frames have a size of $6\times6$ mm but show only a quarter of the numerical grid. (c) shows schematically the instantaneous 2D spatial spectrum of the pattern. The dashed arrow indicates the direction of drift.

grid points. The results were checked on a mesh with $256\times256$ points.

Simulations reveal different kinds of patterns with varying control parameters. For the parameters of Fig. 2, we find a traveling rectangle (TR) structure in the region, in which only the Hopf modes are unstable. Two snapshots of this drifting structure (with the temporal interval between them being half a period) are presented in Figs. 5(a) and 5(b). Figure 5(c) shows a schematic diagram of the pattern in Fourier space. A dashed arrow indicates the direction of the drift of the pattern. Traveling rectangles are known to be one of several spatiotemporal structures produced by a Hopf bifurcation on a plane [28]. With increased pumping we enter the domain of the static instability where the traveling rectangles give way to a state of spatiotemporal irregularity, which we will call turbulent ($T$) in the following. A further increase of the pump leads to the formation of static rolls ($R$) and, in the vicinity of the right edge of the static instability interval in Fig. 2, negative hexagons ($H\pi$). For the parameters of Fig. 3(b), where zones of static and Hopf instabilities overlap, we observed always turbulent behavior.

We have presented results for the case of positive detuning $\bar{\Delta}$, but the same regularities (turbulent behavior at the equal wave numbers of the excited Hopf and static modes) have been found also for negative $\bar{\Delta}$.

### B. Positive longitudinal magnetic field and detuning: $\Omega_z>0,\bar{\Delta}>0$

For a nonzero magnetic field there are two rather different situations. If the signs of the detuning and the longitudinal magnetic field are opposite, the steady-state characteristic is not altered qualitatively compared to the one for zero longitudinal field (Fig. 2) and no qualitatively new dynamics arise. On the other hand, if the detuning and the longitudinal magnetic field have the same sign, one can see from the expression for the steady-state orientation (7) that a resonance effect takes place at $\Omega_z=\bar{\Delta}P_s$, i.e., when the magnetically induced level splitting is compensated by a light induced level shift $\bar{\Delta}P_s$ [18]. Figure 6 displays an example of such a resonancelike behavior: A rather pronounced dip is superimposed on the usual characteristic of a saturable medium. Intervals of linear instability versus formation of static patterns are found on both wings of the resonance. Due to the nonmonotonous dependence $w_s(P_0)$ the sodium vapor behaves as self-defocusing (focusing) medium in the intervals with negative (positive) slope. As a consequence of this, the structures emerging on the left wing of the resonance have a smaller spatial length scale than the patterns on the right wing.

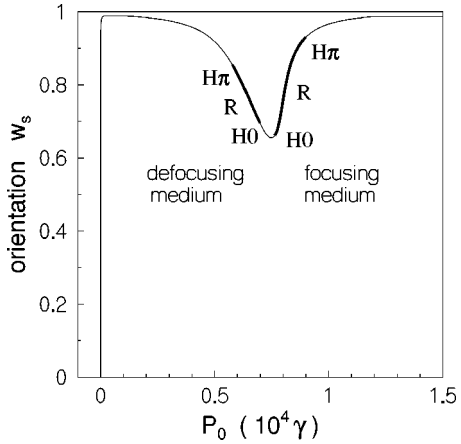


FIG. 6. Steady-state orientation $w_s$ versus external pump rate for the parameters: $\bar{\Delta}=8$, $R=0.915$, $l=15$ mm, $\Omega_z/2\pi=100$ kHz, $\Omega_x/2\pi=9$ kHz, $N=2\times10^{13}$ cm$^{-3}$, $d=100$ mm, $D=100$ mm$^2$/sec. The intervals with static instability are marked by thick solid lines, $H0$—positive hexagons.

With increasing effective nonlinearity (achieved here by increasing the particle density $N$) the shape of the resonance changes (Fig. 7) and becomes bistable after the emergence of two saddle-node bifurcation points [18]. The steady-state characteristic shows the properties attributed to a classical nonlinear resonance [29,30]. The instability interval at the right side of the resonance (the self-focusing part of the characteristic) is split now into two domains II and III. In addition to the static instabilities (domain I) we find that in the immediate vicinity of the resonance a Hopf instability occurs (diamonds in Fig. 7). The insertion of Fig. 7 reveals that the Hopf instability interval links the partitions of static instabilities on both sides of the resonance.

Let us consider the stability properties for the parameters of Fig. 7 in more detail. Figure 8 presents the marginal stability curves in the plane spanned by the parameters $P_0$ and $k_\perp$, where $k_\perp$ is the wave number of the structure.

One can see from Fig. 8 that the wave number of the Hopf structures in the defocusing branch nearly coincides with the size predicted for the static structures on the focusing branch. In addition the ratio between the wave vectors of the Hopf and static modes of domain I is such that two Hopf modes with frequencies $\Omega_H$ and $-\Omega_H$ and with smallest wave num-

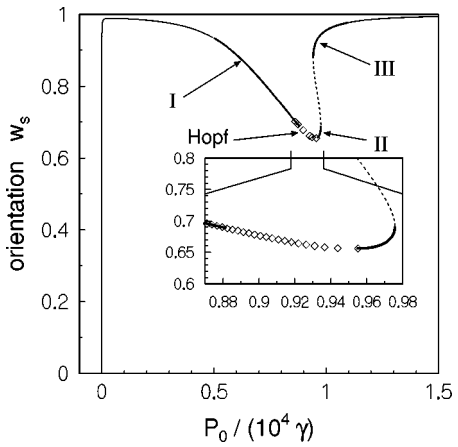


FIG. 7. Steady-state characteristic for $N=8\times10^{13}$ cm$^{-3}$, $D=200$ mm$^2$/sec, and other parameters as in Fig. 6. The intervals with linear instability against static perturbations I, II, and III are marked by thick solid lines, diamonds mark the interval of the Hopf instability. The insertion shows an enlargement of the characteristic in the vicinity of the lowest point of the resonance.

bers can build a static mode with larger wave number through quadratic coupling.

When the external pumping is increased above threshold for the instability domain I, numerical simulations show stationary negative hexagons which give way to stationary stripes and positive hexagons for larger values of the pump. The length scale of the patterns coincides with that predicted by the linear stability analysis (cf. Fig. 8). If the pumping is increased further up to the level where the Hopf instability and the I-static instability coexist, we find nontrivial patterns produced by the resonant interaction between the Hopf and static modes. One such resonant pattern is the *winking hexagons* described in Ref. [13]. Let us recall briefly that winking hexagons are formed through the resonant interaction of two (Hopf and static) triads of modes. The spatiotemporal behavior of this pattern is transparent from the explicit expression for the orientation distribution

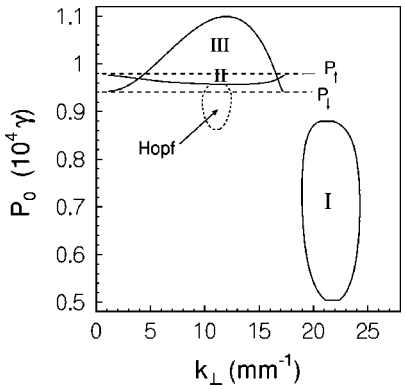


FIG. 8. Neutral stability curves in the plane $(P_0,k_\perp)$ for the parameters of Fig. 7. $P_\uparrow$ and $P_\downarrow$ mark the limit points of the homogeneous solution. The domains of the static (Hopf) instability are bounded by solid (dashed) lines.

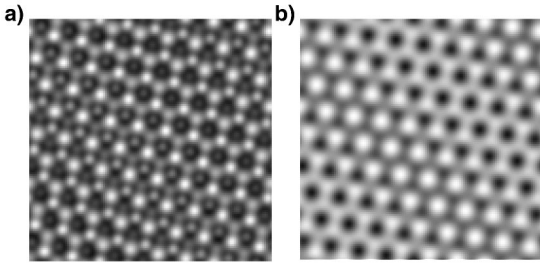


FIG. 9. (a) A snapshot of a nonperfect winking hexagon pattern obtained for $P_0=0.888\gamma\times10^4$ and (b) the pattern constructed only from the Hopf components of the pattern in (a). The frames have a size of 2.5×2.5 mm but show only a quarter of the numerical grid.

$$w=w_s+\sum_{i=1}^{3}\left[A_i e^{i\phi_i+i\Omega_H t}\,\exp(i\boldsymbol{k}_i\cdot\boldsymbol{r}_\perp)\right.$$
$$\left.+B_i e^{i\psi_i}\,\exp(i\boldsymbol{q}_i\cdot\boldsymbol{r}_\perp)+\text{c.c.}\right], \qquad (12)$$

where $A_i$ ($\phi_i$) and $B_i$ ($\psi_i$) are the real amplitudes (phases) of the Hopf and static modes, respectively. Referring to Fig. 1, the wave vectors of the static modes coincide with the harmonics of the Hopf modes, i.e., $\boldsymbol{q}_i=\boldsymbol{k}_i-\boldsymbol{k}_{(i+2)\text{mod}3}$. Our simulations show that they only develop in a small parameter region in which the static modes are either weakly active or weakly (linearly) damped (the case shown in Figs. 7, 8 [33]). The latter case was recently discussed in the framework of amplitude equations [34] and it was shown that in this case patterns composed of resonantly coupled static and Hopf modes can be stabilized already by quadratic interactions. The authors mention that cubic interactions might provide a stabilization also in the case that both mode families are linearly active. Our simulations indicate that—at least in the system considered by us—this parameter region is present but very limited.

In [13] we considered the case of perfect winking hexagons, for which the sum of the phases of the three Hopf modes is constant over the transverse plane and changes like $\Omega_H t$ with time. Here in Fig. 9(a) we present a snapshot of nonperfect winking hexagons. This pattern has been obtained for the same parameters as the perfect winking hexagons with the difference being only the initial transverse distribution of the magnetization. It can be seen that the form of the pattern differs in different spatial domains. The structure of the ''defects'' becomes evident if we analyze the pattern presented in Fig. 9(b) which contains only the Hopf modes. [This pattern has been obtained from that in Fig. 9(a) by filtering all modes in Fourier space excluding the Hopf ones.] The stripes of positive and negative hexagons in Fig. 9(b) witness that the sum of the three Hopf modes varies through the patterns from zero (positive hexagons, i.e., bright peaks on a dark background) to $\pi$ (negative hexagons, i.e., dark dips in a bright background). The time evolution of the pattern in Fig. 9(a) obeys the same regularities as described in [13] for perfect winking hexagons. Let us note that there is a striking similarity between our nonperfect winking hexagon pattern and the transient phason obtained by Müller in a Faraday experiment (cf. Fig. 5 from [31]).

Winking hexagons exist only in a rather narrow interval of the pump parameter. For a slight increase of $P_0$ a

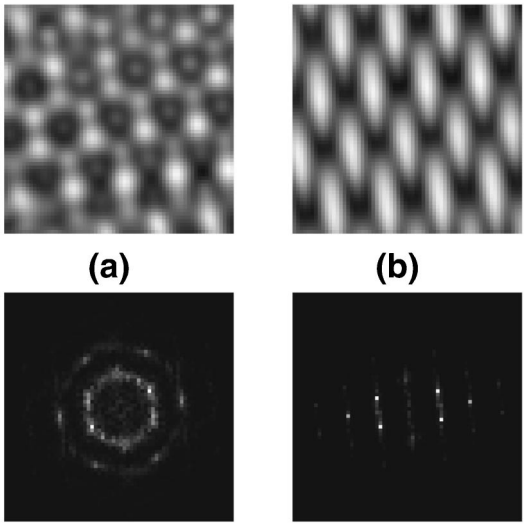


FIG. 10. Snapshots illustrating the decay of the winking hexagon pattern by a slight increase of the pump parameter to $P_0 = 0.9\gamma \times 10^4$. The upper row presents the distribution of the orientation in real space (frame size 2.5×2.5 mm), the lower row the corresponding spatial spectrum (frame size 80×80 $mm^{-1}$). (a) presents the remnants of the winking hexagons; (b) a triadic Hopf-static pattern. The patterns in real space show only one quarter of the numerical grid.

winking-hexagon-like structure [Fig. 10(a)] is unstable and decays. In the course of time, the structure evolves to a drifting rhomb pattern. A snapshot is shown in Fig. 10(b). Recently such drifting rhombs were named *triadic Hopf-static patterns* [12], because they are composed of three (two Hopf and one static) modes. Returning to Fig. 1 one can see that the two Hopf modes are locked through quadratic coupling with the static mode. To our knowledge, spontaneously drifting triadic Hopf-static patterns have not been observed up to now experimentally in systems with rotational symmetry, but only in situations in which the drift was induced by a tilt of the feedback mirror [32]. The triadic Hopf-static pattern appears to be only transient in this situation, though it is found to be stable for other parameters. Finally, the structure evolves to the asymptotically stable state of Fig. 11. The two very bright spots in the right upper corner of Fig. 11(a) are localized states which are excited due to the static instability of the domain II (cf. Figs. 7, 8). As can be seen in Fig. 11(a) the localized states are inserted in the low-amplitude nonstationary background formed by winking hexagons. [The bright peaks in the Fourier spectrum of Fig. 11(b) correspond to the amplitudes of the Hopf and the $\sqrt{3}$-static modes.] With further increasing $P_0$ the number of localized states grows and they build a hexagonal lattice with a length scale as predicted by the linear stability analysis for the domain II of Fig. 8. A detailed investigation of this fairly complicated situation is postponed to a future paper.

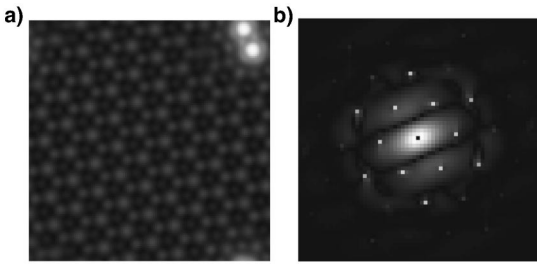


FIG. 11. (a) White-gray plot of the the final pattern and (b) its 2D Fourier spectrum after the transient (displayed in Fig. 10) illustrating the formation of localized states on the nonstationary background of the winking hexagons. The frame size in (a) is 5×5 mm, in (b) 80×80 $mm^{-1}$.

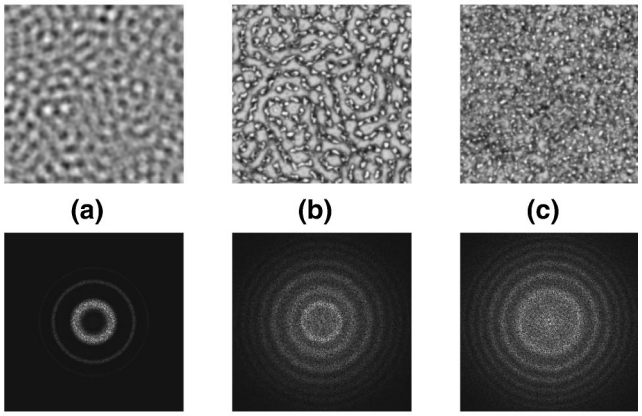


FIG. 12. Time evolution of the turbulent pattern (top) and its spatial Fourier spectrum (bottom) for the parameters of $\bar{\Delta} = -8$, $\Omega_z/2\pi = -100$ kHz, $\Omega_x/2\pi = 10$ kHz, $l = 15$ mm, $N = 10^{14}$ $cm^{-3}$, $d = 400$ mm, $D = 200$ $mm^2$/sec at the instants of time $t$: (a) $t = 0.05$ msec, (b) $t = 0.083$ msec, (c) $t = 0.5$ msec. The patterns in real space show only one quarter of the numerical grid. The frame size in real space is 12.5×12.5 mm, in Fourier space 64×64 $mm^{-1}$.

Concerning the description of hybrid Hopf-static patterns with the help of amplitude equations, it should be emphasized that the terms responsible for coherent mode coupling should be kept. [E.g., in terms of Fig. 1 the time evolution of the amplitude of the static mode $B_1(\boldsymbol{q}_1)$ is influenced by the term $A_1(\boldsymbol{k}_1)A_2(\boldsymbol{k}_2)$, and one Hopf mode is related to the other Hopf modes via interaction with the static mode.] The consequences of these contributions have been considered only recently [3,12,7,34].

### C. Negative longitudinal magnetic field and detuning: $\Omega_z < 0, \bar{\Delta} < 0$

The simultaneous change of the signs of $\Omega_z$ and $\bar{\Delta}$ does not affect the steady-state characteristic given by Eq. (7). However, the stability properties change such that the inner circle in Fig. 1 corresponds now to the static instability whereas the outer circle corresponds to the Hopf instability. Contrary to the case of positive $\Omega_z$ and $\bar{\Delta}$, *a quadratic coupling of the two static modes cannot give the Hopf mode*. As a consequence, spatiotemporal phase matching cannot be achieved. Numerical simulations for this case show that the simultaneous excitement of the Hopf and static modes leads to the development of spatiotemporal turbulence. Figure 12 illustrates the time evolution of the turbulent state from the corresponding homogeneous steady state in which the atomic variables are randomized over the spatial grid. Figure 12(a) shows a snapshot in the initial stage of the development where the static modes are most pronounced in the spatial spectrum [lower part of Fig. 12(a)]. With evolving time more and more spatial frequencies are excited [Fig. 12(b)] and the

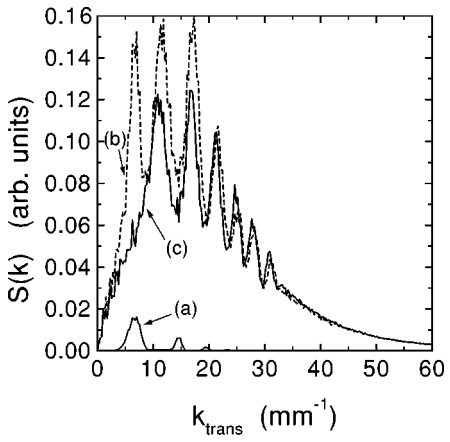


FIG. 13. Dynamics of the spatial spectra obtained from the data presented in the lower part of Fig. 12 by integrating over the polar coordinate.

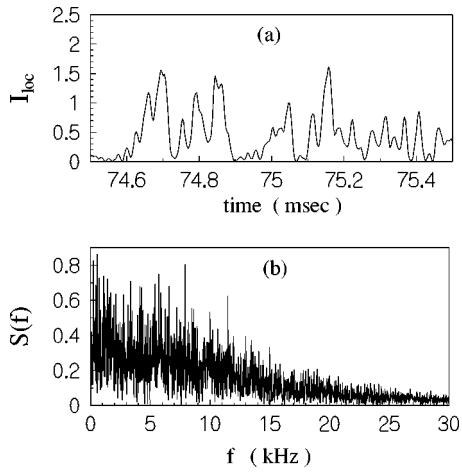


FIG. 14. (a) Fragment of the temporal evolution of the local intensity of the transmitted light and (b) the Fourier spectrum calculated from the full time series.

Hopf modes appear to be dominant. The last picture of the series [Fig. 12(c)] shows a snapshot of the asymptotic turbulent state. Characterizing the turbulent behavior one can say that small and large bright spots (and clouds of spots) are in disordered motion whereas the spectrum [lower part of Fig. 12(c)] maintains its main features.

To see the development of the spatial frequencies more clearly we present in Fig. 13 amplitude spectra which just depend on the modulus of the wave vector. They are obtained from the data presented in the lower part of Fig. 12 by integrating over the polar coordinate. In the initial stage essentially only one peak [curve (a) in Fig. 13] is present, which is due to the development of the static instability. Later, along with the static peak, the Hopf peak [the next peak to the right from the static one in curve (b)] grows. Many other peaks appear. Presumably, this is due to the self- and cross-interaction between the different modes, since the distance between the peaks corresponds roughly to the difference in wave number between the Hopf and the static modes. In the process of competition the Hopf instability wins and the curve (c) in Fig. 13 (corresponding to the turbulent state) shows that the peak with the highest excitation is the Hopf one. The spectra are found to be insensitive to the details of the numerics (number of mesh points, size of transverse area).

An example of the temporal characteristics of the turbulent behavior for these parameters is presented in Fig. 14. The time dependence of the intensity of the light transmitted through the cell is shown in Fig. 14(a). We have determined the local intensity in one point of the grid imitating a small detector in the experiment. One can see that the light intensity pulsates rather *irregularly*, which is confirmed by the temporal Fourier spectrum in Fig. 14(b). Note that the spectrum has no visible local maximum for the Hopf frequency predicted by the linear stability analysis.

The described main features of the observed spatiotemporal chaotic behavior give us the arguments to refer to it as *amplitude turbulence* [35,36].

Figure 15 provides an overview over the bifurcation behavior in the $(P_0\text{-}d)$ space. The point (denoted by $A$) for which the behavior was just discussed is well inside the region with turbulent behavior. As is apparent from the diagram, the Hopf bifurcation takes place only for rather high values of the cell-to-mirror distance. This dependence on $d$ can be understood by the fact that the Hopf modes are damped more strongly by diffusion than the static ones, since their wave number is larger. The damping is smaller and less important for high $d$ (cf. the discussion at the end of Sec. II). For a small mirror distance secondary bifurcations to stationary structures occur which are discussed in more detail in [15,17]. Note that the turbulent region extends beyond the borders of the domain in which the Hopf modes are unstable. This is possibly due to the fact that the Hopf modes are only slightly damped here.

## IV. CONCLUSION

We have examined three different situations: (i) the Hopf and the static modes are of the same spatial wave number; (ii) the wave number of the Hopf mode is smaller than the one of the static one so that the sum of two Hopf modes can resonate with a static mode; (iii) the wave number of the static mode is smaller than the one of the Hopf mode. Based

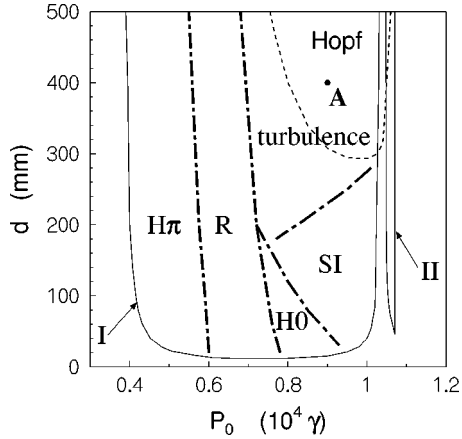


FIG. 15. Bifurcation diagram in the plane of control parameters $(P_0,d)$ for the parameters $\Omega_z/2\pi=-100$ kHz, $\Omega_x/2\pi=10$ kHz, $\bar{\Delta}=-8$, $N=10^{14}$ cm$^{-3}$. Solid lines enclose the two domains I and II of static instability, the area with a Hopf instability is bounded by the fine dashed line. Different regimes found in simulatons are separated by the thick dashed lines (SI—secondary instabilities).

on the findings we can draw the following conclusions. Each one taken alone for itself—both Hopf and static modes—can build regular patterns. However, only in case (ii) does the interplay of simultaneously excited Hopf and static modes lead to regular spatiotemporal structures. In cases (i) and (iii) the interaction of instabilities gives rise to spatiotemporal turbulence. The latter fact confirms the results obtained in other pattern-forming systems [19–23].

## ACKNOWLEDGMENTS

The authors thank W. Lange and B. Schäpers for numerous fruitful discussions.

## APPENDIX LINEAR STABILITY ANALYSIS

$$a_0=[\gamma_{\rm eff}^2+(\Omega_z-\overline{\Delta}P_s)^2][\gamma_{\rm eff}-(1-w_s)\Xi]+\gamma_{\rm eff}\Omega_x[\Omega_x+(v_s+\overline{\Delta}u_s)\Xi]-\Omega_x(\Omega_z-\overline{\Delta}P_s)(\overline{\Delta}v_s-u_s)\Xi,$$

$$a_1=3\gamma_{\rm eff}^2-2\gamma_{\rm eff}(1-w_s)\Xi+\Omega_x[\Omega_x+(v_s+\overline{\Delta}u_s)\Xi]+(\Omega_z-\overline{\Delta}P_s)^2,$$

$$a_2=3\gamma_{\rm eff}-(1-w_s)\Xi,$$

where

$$\gamma_{\rm eff}=\gamma+P_s+Dk_\perp^2,$$

$$\Xi=-RP_0\ {\rm Re}(\chi_{\rm lin})kl\left|e^{[-ikl\chi_{\rm lin}(1-w_s)]/2}\right|^2\times\left[\sin\left(\frac{k_\perp^2 d}{k}\right)+\frac{1}{\overline{\Delta}}\cos\left(\frac{k_\perp^2 d}{k}\right)\right].$$


[1] I. Mutabazi and C. D. Andereck, Phys. Rev. E **51**, 4380 (1995).
[2] H. R. Brand and R. J. Deissler, Phys. Lett. A **231**, 179 (1997).
[3] A. De Wit, D. Lima, G. Dewel, and P. Borckmans, Phys. Rev. E **54**, 261 (1996).
[4] N. D. Mermin and S. M. Troian, Phys. Rev. Lett. **54**, 1524 (1985).
[5] H. W. Müller, Phys. Rev. E **49**, 1273 (1994).
[6] T. Frisch and G. Sonnino, Phys. Rev. E **51**, 1169 (1995).
[7] E. V. Degtyarev and M. A. Vorontsov, J. Mod. Opt. **43**, 93 (1996).
[8] W. J. Firth, J. Mod. Opt. **37**, 151 (1990).
[9] G. D'Alessandro and W. J. Firth, Phys. Rev. A **46**, 537 (1992).
[10] M. Le Berre, D. Leduc, E. Ressayre, and A. Tallet, Phys. Rev. A **54**, 3428 (1996).
[11] E. Pampaloni, S. Residori, S. Soria, and F. T. Arecchi, Phys. Rev. Lett. **78**, 1042 (1997).
[12] Yu. A. Logvin, B. A. Samson, A. A. Afanas'ev, A. M. Samson, and N. A. Loiko, Phys. Rev. E **54**, R4548 (1996).
[13] Yu. A. Logvin, T. Ackemann, and W. Lange, Europhys. Lett. **38**, 583 (1997).
[14] F. Mitschke, R. Deserno, W. Lange, and J. Mlynek, Phys. Rev. A **33**, 3219 (1986).
[15] T. Ackemann, Yu. A. Logvin, A. Heuer, and W. Lange, Phys. Rev. Lett. **75**, 3450 (1995).
[16] W. Lange, Yu. A. Logvin, and T. Ackemann, Physica D **96**, 230 (1996).
[17] Yu. A. Logvin, T. Ackemann, and W. Lange, Phys. Rev. A **55**, 4538 (1997).
[18] T. Ackemann, A. Heuer, Yu. A. Logvin, and W. Lange, Phys. Rev. A **56**, 2321 (1997).
[19] A. De Wit, G. Dewel, and P. Borckmans, Phys. Rev. E **48**, R4191 (1993).
[20] P. De Kepper, J.-J. Perraud, B. Rudovics, and E. Dulos, Int. J. Bifurcation Chaos Appl. Sci. Eng. **4**, 1215 (1994).
[21] J. Boissonade, E. Dulos, and P. De Kepper, in *Chemical Waves and Patterns*, edited by R. Kapral and K. Showalter (Kluwer, Dordrecht, 1995), p. 221.
[22] J. E. Pearson, Science **261**, 189 (1993).
[23] J. Danckaert and G. Vitrant, Opt. Commun. **104**, 196 (1993).
[24] M. Tamburrini, E. Ciaramella, and E. Santamato, Chaos Solitons Fractals **4**, 1355 (1994).
[25] M. Kitano, T. Yabuzaki, and T. Ogawa, Phys. Rev. A **24**, 3156 (1981).
[26] F. Mitschke, J. Mlynek, and W. Lange, Phys. Rev. Lett. **50**, 1160 (1983).
[27] M. Möller and W. Lange, Phys. Rev. A **49**, 4161 (1994).
[28] M. Silber, H. Riecke, and L. Kramer, Physica D **61**, 260 (1992).
[29] L. D. Landau and E. M. Lifshitz, *Mechanics* (Pergamon, Oxford, 1976).
[30] B. A. Huberman and J. P. Crutchfield, Phys. Rev. Lett. **43**, 1743 (1979); D. D'Humieres, M. R. Beasley, B. A. Huberman, and A. Libchaber, Phys. Rev. A **26**, 3483 (1982); Yu. A. Logvin, A. M. Samson, and S. I. Turovets, Opt. Commun. **84**, 99 (1991).
[31] H. W. Müller, Phys. Rev. Lett. **71**, 3287 (1993).
[32] B. Schäpers, T. Ackemann, and W. Lange (unpublished).
[33] The same applies to the simulations reported in [13]. Figure 2 of [13] depicts by mistake the situation for $D=100\ {\rm mm}^2/{\rm s}$.
[34] B. Y. Rubinstein and L. M. Pismen, Phys. Rev. A **56**, 4264 (1997).
[35] M. C. Cross and P. C. Hohenberg, Rev. Mod. Phys. **65**, 851 (1993).
[36] M. V. Bazhenov, M. I. Rabinovich, and A. L. Fabrikant, Phys. Lett. A **163**, 87 (1992); M. I. Rabinovich, A. L. Fabrikant, and L. S. Tsimring, Usp. Fiz. Nauk **162**, 1 (1992) [Sov. Phys. Usp. **35**, 629 (1992)].